POLITECNICO DI TORINO
Repository ISTITUZIONALE

On the scaling of large-scale structures in smooth-bed turbulent open-channel flows

Original
On the scaling of large-scale structures in smooth-bed turbulent open-channel flows / Peruzzi, C., Poggi, D., Ridolfi, L., Manes, C.. - In: JOURNAL OF FLUID MECHANICS. - ISSN 0022-1120. - ELETTRONICO. - 889:(2020). [10.1017/jfm.2020.73]

Availability:
This version is available at: 11583/2796577 since: 2020-02-22T21:17:15Z

Publisher:
Cambridge University Press

Published
DOI:10.1017/jfm.2020.73

Terms of use:

This article is made available under terms and conditions as specified in the corresponding bibliographic description in the repository

Publisher copyright

(Article begins on next page)

26 November 2026

On the Scaling of Large-Scale Structures in Smooth-Bed Turbulent Open-Channel Flows

C. Peruzzi[1]†, D. Poggi[1], L. Ridolfi[1], and C. Manes[1]

[1]Department of Environmental, Land and Infrastructure Engineering, Politecnico di Torino, 10129 Turin, Italy

(Received xx; revised xx; accepted xx)

This paper investigates the existence and scaling of the so-called Large- and Very-Large-Scale Motions (i.e. LSMs and VLSMs), in non-uniform turbulent open-channel flows developing over a smooth-bed in a laboratory flume. A Laser Doppler Anemometry system was employed to measure vertical profiles of longitudinal and bed-normal velocity statistics over a wide range of hydraulic conditions. Pre-multiplied spectra of the longitudinal velocity fluctuations revealed the existence of two peaks occurring at wavelengths consistent with those associated with LSMs and VLSMs as detected in the past literature pertaining to wall turbulence. However, contrary to so-called canonical wall-flows (i.e. flat plate boundary layers, pipe and closed-channel flows), LSM- and VLSM-peaks observed in the open-channel flows investigated herein, are detectable over a much larger extent of the wall-normal coordinate. Furthermore, the VLSM-peak appears at von Kàrmàn numbers Re_τ as low as 725, whereas in other wall-flows much higher values are normally required. Finally, as conjectured by a recent study on uniform, rough-bed open-channel flows, the present paper confirms that LSM-wavelengths scale nicely with the flow depth, whereas the channel aspect ratio (i.e. the ratio between channel width and flow depth) is the non-dimensional parameter controlling the scaling of VLSMs-wavelengths. The intensity and wavelengths of the VLSM-peaks were also observed to be dependent on the spanwise coordinate. This result suggests that VLSMs might be dynamically linked to secondary currents as these are also known to vary in strength and size across the channel width.

Key words:

1. Introduction

In wall-flows, the study of large-scale coherent structures has received particular attention because such structures carry a large portion of the Turbulent Kinetic Energy (TKE) and contribute significantly to the transport of momentum and relevant scalars such as heat, oxygen and pollutants (Robinson 1991; Marusic *et al.* 2010; Jiménez 2018). There is now compelling evidence that, in canonical smooth-wall flows - which include (flat-plate) turbulent boundary layers, closed-channel and pipe flows - two distinct large-scale structures occur, which are commonly referred to as Large-Scale Motions (LSM) and Very-Large-Scale Motions (VLSM). While there are several methods to visualise and identify such structures, the most employed diagnostic tool is based on pre-multiplied one-dimensional spectra, where LSMs and VLSMs impose two well-defined

† Email address for correspondence: cosimo.peruzzi@polito.it

peaks (Kim & Adrian 1999; Hutchins & Marusic 2007*b*). Many studies have proven that such peaks occur at wavenumbers which scale with the characteristic outer length-scale of the flow δ (Kim & Adrian 1999; Adrian *et al.* 2000; Del Álamo & Jiménez 2003; Ganapathisubramani *et al.* 2003; Tomkins & Adrian 2003; Hutchins *et al.* 2005; Guala *et al.* 2006; Balakumar & Adrian 2007; Hutchins & Marusic 2007*a*,*b*; Monty *et al.* 2007, 2009; Sillero *et al.* 2014; De Silva *et al.* 2018).

In order to obtain a clear distinction between the two aforementioned peaks, though, Hutchins & Marusic (2007*b*) recommend that the von Kàrmàn number $Re_\tau = \delta u_\tau/\nu$ (where u_τ is the shear velocity and ν is the kinematic viscosity) of the flow should not be less than 1700. This number is a reference value that ensures one order of magnitude of length-scale separation between LSMs and VLSMs in turbulent boundary layers. When this condition is satisfied, Hutchins & Marusic (2007*a*,*b*) showed that, wavenumbers associated with LSM and VLSM peaks, correspond to structures whose longitudinal size is $2-3\delta$ and 6δ, respectively. It was also observed that LSM-peaks persist throughout most of the outer layer while VLSM-peaks vanish above the logarithmic region.

As far as pipe and channel flows are concerned, the picture is significantly different from boundary layers because spectral peaks corresponding to VLSMs are detectable well within the outer layer (Monty *et al.* 2007, 2009; Sillero *et al.* 2014) and correspond to scales up to 20δ. More similarly to turbulent boundary layers, LSM-peaks were observed to scale as 3δ and to persist up to the channel/pipe centreline (see also Kim & Adrian 1999; Guala *et al.* 2006; Balakumar & Adrian 2007).

About the generation mechanism of LSMs and VLSMs, the literature proposes two potential explanations associated with two approaches. There is a so-called "parent-offspring" approach whereby LSMs are considered to emerge out of the alignment of hairpin-vortex packets and VLSMs, in turn, as groups of aligned LSM packets (Hommema & Adrian 2002; Adrian 2007; Adrian & Marusic 2012; Katul 2019). The second approach, instead, claims that VLSMs and LSMs are a direct consequence of a mean-flow instability process and their existence is independent of the dynamics of smaller-scale structures, such as hairpin vortices, which, in the first approach, are instead considered as the building-block of wall-turbulence (Hwang & Cossu 2010). In the second approach, given their streaky and meandering nature and their marked longitudinal vorticity, VLSMs are interpreted to be the principal actors of a self-sustaining "outer-layer" cycle, which shares analogies with its better understood near-wall (i.e. in the buffer layer) counterpart, where VLSMs play the same role as the so-called elongated streamwise vortices (Rawat *et al.* 2015; Hwang & Bengana 2016; Hwang *et al.* 2016; Cossu & Hwang 2017).

Large-scale coherent structures have been extensively studied also in open-channel flows, which are the subject of the present study, as they influence ecologically-relevant scalar transport processes (such as oxygen, nutrients and sediments), river morphodynamics and even the power output of hydro-kinetic marine turbines (Moog & Jirka 1999; Jirka *et al.* 2010; Nepf 2012; Venditti *et al.* 2013; Chamorro *et al.* 2013; Trinci *et al.* 2017; Cameron *et al.* 2019). Laboratory and field experiments have detected the presence of large-scale wedge-type structures, whose sizes in the streamwise, spanwise and wall-normal direction is expressed as a function of the outer-scale, namely, the water depth h (Jackson 1976; Nakagawa & Nezu 1981; Rashidi & Banerjee 1988; Nezu & Nakagawa 1993; Rashidi 1997; Tamburrino & Gulliver 1999; Shen & Lemmin 1999; Shvidchenko & Pender 2001; Cellino & Lemmin 2004; Roy *et al.* 2004; Hurther *et al.* 2007; Franca & Lemmin 2015; Zhong *et al.* 2016; Da Silva & Yalin 2017; Bagherimiyab & Lemmin 2018; Ghesemi *et al.* 2019).

Although some studies indicate the presence of long structures with streamwise vorticity, which resemble the VLSMs as defined in canonical flows (Grinvald & Nikora 1988;

Nezu 2005; Sukhodolov *et al.* 2011; Zhong *et al.* 2015), Cameron *et al.* (2017) were the first to provide insights into the occurrence and scaling of VLSMs in turbulent open-channel flows. In this study, the authors present long-duration Particle Image Velocimetry (PIV) measurements in fully-rough open-channel flows over a bed made of spheres packed in a hexagonal arrangement. Among the numerous results, they report pre-multiplied spectra of the longitudinal velocity component, which display the characteristic double-peak behaviour observed for canonical wall-flows. They also report that one of the peaks occurs at wavelengths of about $6-7h$ and nicely scales with the water depth. This peak was associated with the presence of LSMs. The other peak occurred at wavelengths consistent with those pertaining to VLSMs, but not scaling with the flow depth. Moreover, such wavelengths were recorded to be up to 50 times the water depth h. If h is taken as the representative outer length-scale (as it is normally assumed), this means that the non-dimensional length of VLSMs in open-channels flows (as detected from pre-multiplied spectral peaks) is much greater than in other canonical wall-flows. Due to the mismatch between the VLSM and LSM scaling, the authors concluded that, in open-channel flows, these two types of structures might be generated by independent and, possibly, different mechanisms.

Unfortunately, due to the fact that the experiments were performed in rough-wall conditions, Cameron *et al.* (2017) could not unambiguously identify the non-dimensional parameter controlling the scaling of VLSMs among the following: the aspect ratio W/h, the relative submergence h/D and the von Kàrmàn number Re_τ (where W is the channel width and D is the spheres' diameter). The number of factors further increased when, in a subsequent study, the same authors (Cameron *et al.* 2018) noticed that VLSMs wavelengths were also dependent on the non-dimensional distance from the flume inlet x/h. Despite the large number of parameters involved, Cameron *et al.* (2017) argued that the aspect ratio W/h was the most plausible "culprit" for the variation of depth-normalised VLSM wavelengths. The authors justify this hypothesis on the basis that VLSMs and W are of the same order of magnitude and hence W might constrain VLSMs' growth.

The main aim of the present work is to further explore the scaling of LSMs and VLSMs in open-channel flows. Towards this end, we present results from a series of smooth-bed experiments, as they are free from complicating factors associated with rough-beds. In fact, in smooth-bed open-channel flows, the number of non-dimensional parameters that may influence the scaling of large-scale structures reduce from four to three, namely Re_τ, W/h and x/h. It should be emphasized that the experiments reported herein were carried out in non-uniform flow conditions, which can represent a potential complicating factor. As extensively discussed in the next section, though, non-uniformity levels were kept mild and constrained within a limited range. Besides guaranteeing for self-similar flow conditions to be established, this allowed for a comparative analysis between different tests, where the effects of Re_τ, W/h and x/h on velocity statistics (with a specific focus on velocity spectra) could be reasonably isolated and explored.

After this Introduction, the present paper is structured as following: section 2 outlines the experimental methodology; section 3 reports and describes the results coming from velocity measurements and is splitted in two parts: section 3.1 presents classical one-point velocity statistics and section 3.2 presents and discusses the core of the results via spectral analysis; section 4 is devoted to conclusions.

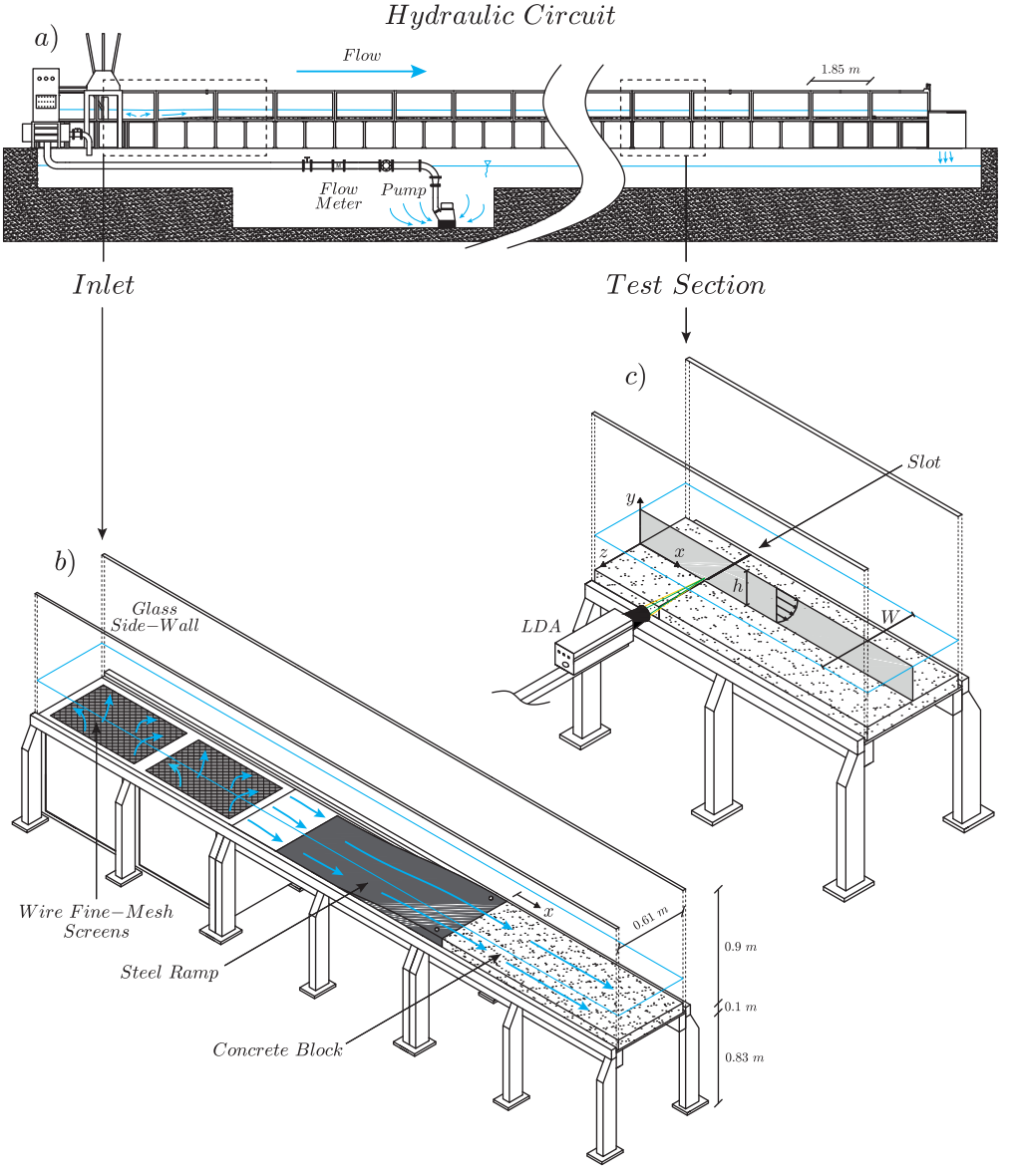


FIGURE 1. Overview of the flume used for the experiments: (a) sketch of the whole hydraulic circuit; (b) and (c) details of the inlet flow conditions and the test section, respectively. Panel (c) also shows the system of coordinate axes chosen in the present study (i.e. the streamwise x, wall-normal y and spanwise z directions) and define the flow depth h and the channel width W. Please note that the coordinate x has it origin at the downstream end of the ramp (see panel b).

2. Experimental Methodology

2.1. *Experimental set-up*

Experiments were carried out in a large-scale, non-tilting, recirculating, open-channel flume at the Hydraulics Laboratory of the Politecnico di Torino (figure 1a). The main part of the facility is composed of a rectangular channel, which is 50 m long, 0.61 m wide and 1 m deep. The flume has glass side-walls and a bed that is made mainly of steel

and in some parts of glass. The flume bottom needed to be raised in order to allow for near-wall LDA measurements, which were carried out following the technique proposed by Poggi *et al.* (2002), described later. To this end, smooth concrete blocks (2 m long, 0.6 m wide and 0.1 m thick) were placed over the original bed of the flume along its entire length. The Nikuradse's equivalent sand roughness k_s for hand-finished concrete without irregularities was estimated to be equal to 0.25 mm (in line with the tabulated values listed in Henderson 1966). In the proximity of the upstream-end of the flume, the original bed and the concrete blocks were gently connected by a stainless steel ramp (1.6 m long) designed to follow the shape of a fifth-degree polynomial (Bell & Mehta 1988) to avoid boundary layer separation (figure 1b). In order to further reduce turbulence generated by the hydraulic circuit, a series of wire fine-mesh screens were placed in the sump underlying the flume inlet (figure 1b). The water depth was regulated by means of a vertical slot-weir placed at the downstream-end of the flume and five ultrasonic distance sensors (company Fae s.r.l., model FA 18-800/I-S) were arranged along the length of the flume in order to monitor the slope of the mean water depth (distances from the x origin: 3.1 m, 21.1 m, 27.1 m, 30.8 m and 39.8 m). Each probe emits an ultrasonic signal, which propagates with a divergence-angle of 8 degrees and is characterized by an optimal sensing distance ranging between 10−80 cm from the sensor. In this specific application, each probe was positioned at 80 cm from the concrete bottom, which means that free-surface fluctuations were measured over an area of 0.025 m^2 for a water depth of 20 cm and over an area of 0.039 m^2 for a water depth of 5 cm. The accuracy of the measured distance is ±1 mm, which results to be a constant value if the gauge works inside the optimal sensing distance.

A digital thermometer (precision of ±0.2 °C) was employed to monitor the temperature of the water and hence estimate its kinematic viscosity ν, for each experiment.

A submerged pump enabled water recirculation between the channel and a large underground sump, which was connected to the inlet through a pipe with diameter 200 mm where an electromagnetic flow-meter was mounted to monitor the flow rate for each experimental test (figure 1a).

As already mentioned, near-wall LDA measurements were made possible by adopting the technique developed and extensively tested by Poggi *et al.* (2002) and subsequently utilised in many other studies (Poggi *et al.* 2003, 2007; Escudier *et al.* 2009; Manes *et al.* 2011). This technique is very simple but effective. It involves the making of a thin vertical slot in the bed that allows for the passage of the vertical LDA laser-beams (figure 1c). To this end, in the proximity of the test section, the vertical slot was created simply by leaving a 3 mm gap between two adjacent concrete blocks. The lower part of the gap was filled by consolidated sand and blocked using Teflon tape. The slot created in this way proved to be effective for the undisturbed propagation of the vertical laser-beams while avoiding measurable alterations of near-wall turbulence properties (see section 3.1).

The instantaneous velocity fluctuations were measured by means of a 2-D LDA working in back-scatter configuration. The LDA system is a Dantec Dynamics Flow Explorer DPSS working with two pairs of laser beams having a wavelength of 532 nm (green) for the longitudinal component (u) and 561 nm (yellow) for the wall-normal component (v). The intersection between these four beams create two ellipsoidal measurement-volumes of $2.96{\cdot}10^{-3}$ mm^3 (ellipsoidal axes: $d_x = 0.083$ mm, $d_y = 0.082$ mm and $d_z = 0.828$ mm) and $2.52{\cdot}10^{-3}$ mm^3 (ellipsoidal axes: $d_x = 0.078$ mm, $d_y = 0.078$ mm and $d_z = 0.785$ mm) for the measurement of u and v, respectively (these estimates are provided by the manufacturer on the basis of the e^{-2} light-intensity cut-off principle, see Dantec Dynamics 2011). The maximum laser power is 300 mW for each pair of laser beams. Signal processing was carried out with two Dantec Dynamics Burst Spectrum

Run	h [cm]	U_b [m/s]	u_τ [m/s]	δ_ν [μm]	l^+ [–]	Re_b [–]	Re_τ [–]	Fr [–]	W/h [–]	x/h [–]	z/W [–]	Symbol
Test 1	20.0	0.2195	0.00985	89.3	9	30150	2240	0.157	3.05	150	0.00	♦
Test 2	15.0	0.3146	0.01432	75.4	11	29310	1990	0.259	4.07	200	0.00	●
Test 3	12.0	0.1517	0.00755	120.1	7	14400	999	0.140	5.08	250	0.00	★
Test 4	10.3	0.4036	0.01836	58.7	14	28800	1752	0.402	5.92	145	0.00	✸
Test 5	10.1	0.4442	0.02016	53.1	15	31510	1904	0.446	6.04	297	0.00	■
Test 5a	10.1	0.4442	0.02016	53.1	15	31510	1904	0.446	6.04	297	0.08	▲
Test 5b	10.1	0.4442	0.02016	53.1	15	31510	1904	0.446	6.04	297	0.16	▶
Test 5c	10.1	0.4442	0.02016	53.1	15	31510	1904	0.446	6.04	297	0.24	▼
Test 5d	10.1	0.4442	0.02016	53.1	15	31510	1904	0.446	6.04	297	0.33	◀
Test 6	8.5	0.4849	0.02221	45.1	18	32180	1886	0.531	7.18	353	0.00	✖
Test 7	5.0	0.2916	0.01518	69.0	12	11960	725	0.414	12.20	600	0.00	✚

TABLE 1. Summary of experiments and associated hydraulic conditions. The columns indicates: the water depth h, the bulk velocity U_b, the shear velocity u_τ, the viscous length scale $\delta_\nu = \nu/u_\tau$ where ν is the kinematic viscosity, the viscous-scaled LDA measurement length $l^+ = d_z u_\tau/\nu$ where d_z is the longest ellipsoidal axis of the LDA measurement volume, the bulk Reynolds number $Re_b = R_h U_b/\nu$ where $R_h = Wh/(W+2h)$ is the hydraulic radius and W is the channel width, the von Kàrmàn number $Re_\tau = hu_\tau/\nu$, the Froude number $Fr = U_b/\sqrt{gh}$ where g is the gravitational acceleration, the aspect ratio W/h and the non-dimensional distance from the inlet x/h. Finally, z/W indicates the normalised spanwise position for the velocity measurements, where z is the spanwise coordinate starting from the flume centreline.

Analyzers (BSA F600-2D) and a dedicated Dantec software (BSA Flow Software v6.5) set up on a local PC network station. Data were always acquired in coincidence mode to allow for the estimation of the Reynolds shear stresses. The sampling frequency f_s was always between 100 Hz and 400 Hz (depending on the hydraulic conditions) and more than 500 000 velocity measurements were collected for each measurement point over a minimum duration of 40 minutes. This amount of data ensured a negligible sampling error for all the statistics presented in section 3.1 (i.e. the sampling error results much smaller than the size of the marker-symbols used in the plots). The LDA optics (Dantec Dynamics 2011) was traversed by means of a 3-D computer-controlled Dantec Dynamics traversing system (ISEL iMC-S8 Traverse) which allows for movements along three directions with a resolution of 6 μm. For each experiment, particular attention was dedicated to ensure that the LDA beams were perfectly aligned with the horizontal and vertical (i.e. gravity) directions. To this end, the flume was filled with water in quiescent conditions (this was possible by sealing the outlet of the flume with a steel cap) so that the resulting free-surface could be used as a perfectly horizontal plane, which was then used as a reference for the four laser-beams alignment. The origin of the vertical coordinates was identified by means of a sharp point gauge connected to a vernier calliper (accuracy of 0.05 mm) and left at a known distance from the bed. The LDA sampling volume was then moved towards the pointer and the backscatter signal monitored with the BSA Flow Software. While gently approaching the sampling volume towards the pointer, the backscatter signal was monitored and when it begun to be disturbed by the pointer, it was assumed that the pointer and the LDA sampling volume coincided and the elevation above the bed recorded as a reference to identify the origin of the vertical axis. By repeating this method for multiple heights above the bed, it was observed that the zero reference level could be detected with an accuracy of about ± 0.1 mm (in wall units this uncertainty varies according to the test, with an averaged value of ± 1.5).

2.2. *Hydraulic conditions*

The main parameters describing the hydraulic conditions associated with each experiment are reported in table 1. All the experiments were carried out with a flat bed as the flume is non-tilting. This clearly implies that all the investigated flows were non-uniform. It is therefore important to specify that all the parameters reported in table 1 refer to flow conditions measured at the test section of each trial.

For most of the experiments, the test section was located at $x = 30$ m (the longitudinal, wall-normal and spanwise coordinates are indicated with x, y and z, and defined as in figure 1c) from the origin of the x coordinate (figure 1b). Test 4 is the only exception as it was carried out at $x = 15$ m, at flow conditions similar to test 5, to investigate and isolate the effects of x/h on VLSMs' scaling, while maintaining constant all the other relevant non-dimensional parameters.

Note that, all the LDA measurements related to tests 1−7 were carried in the central cross-section of the flume (i.e. $z/W = 0$, where z originates in the centreline of the flume, see figure 1c), except for tests 5a−5d (table 1). In these tests, the flow conditions were the same as test 5, but the LDA system was traversed at four spanwise positions across the flume half-width (i.e. $z/W = 0.08$; 0.16; 0.24; 0.33). For each z/W position, LDA measurements were taken over 19 different locations along the bed-normal coordinate. These tests were carried out to quantify the effects of lateral boundaries on the intensity and wavenumber of LSMs and VLSMs peaks in pre-multiplied spectra.

The flow depth h was determined from the ultrasonic gauge positioned in close proximity of the test section by doing the mean of a 30-minutes long time-series. This value was compared with the value read on a high precision ruler (accuracy of 0.5 mm) positioned just next to the LDA. The difference in h measured by means of the two methods was well within both instruments' uncertainty.

Note that tests 1 and 2 were carried out at flow depths corresponding to aspect-ratio values below 5, which is considered the minimum to allow for turbulence statistics in the central cross-section of the flume to be independent of lateral-wall effects (Nezu & Nakagawa 1993). These tests were carried out as they impose extreme "constraining conditions" of the lateral walls to VLSMs. Following the conjecture made by Cameron *et al.* (2017), it is expected that the non-dimensional length of VLSMs for these two tests is significantly lower than those pertaining to the other tests presented herein. It should be pointed out that tests 1 and 2 were made possible thanks to the remarkable length of the flume, which allowed for the development of a boundary layer as deep as the water depth (i.e. up to 20 cm), which is not easy to obtain in standard flumes working in smooth-bed conditions.

The bulk flow velocity U_b is herein defined as the mean fluid velocity averaged over the flow depth, i.e. $U_b = \frac{1}{h}\int_0^h U(y)\,dy$, where $U(y)$ is the time-averaged longitudinal velocity profile measured at the test section.

The shear velocity u_τ was estimated following the procedure outlined in section 2.3. These values were then used to compute the viscous length scale $\delta_\nu = \nu/u_\tau$ and, in turn, the roughness Reynolds number $k_s^+ = k_s/\delta_\nu$, which resulted to be always lower than 5.5, hence indicating hydraulically smooth-bed flow conditions for all the tests.

Table 1 also provides the characteristic length of the LDA sampling volume l normalised with the viscous length scale, $l^+ = l/\delta_\nu$. In an attempt to provide a conservative estimation of l^+, l was taken equal to d_z as it is the largest dimension of the LDA measurement volume. The obtained values of l^+ align with (and in some instances are even lower than) those reported in past studies of wall-turbulence (see e.g. Hutchins *et al.* 2009; Monty *et al.* 2009).

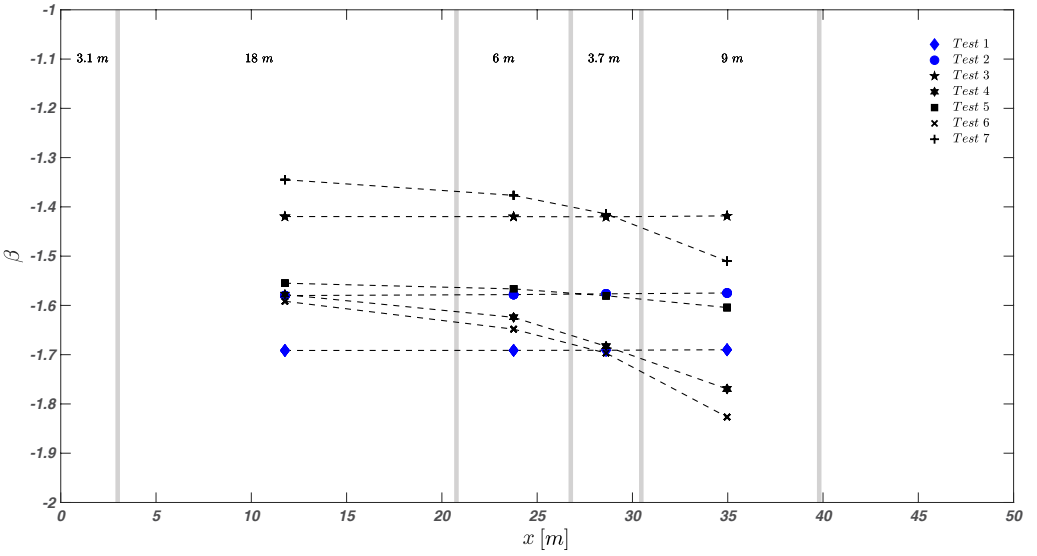


FIGURE 2. Estimated β values along the channel flume. The grey vertical lines indicate the positions of the five ultrasonic gauges.

The level of non-uniformity caused by the flat bed conditions was characterized by means of the parameter β, which was estimated as follows:

$$\beta(x) = \frac{gh(x)}{u_\tau(x)^2}(S_w(x) - S_0), \tag{2.1}$$

where S_0 is the bottom slope (clearly zero due to the flat bed conditions of the flume), $S_w = \mathrm{d}h/\mathrm{d}x$ is the gradient of the free surface and g is the gravitational acceleration. With this definition, $\beta = -1$ indicates uniform flow conditions (i.e. the flow depth has a null gradient along x), $\beta > -1$ indicates decelerating flow conditions (i.e. the flow depth has a positive gradient along x) and $\beta < -1$ stands for accelerating flow conditions (i.e. the flow depth has a negative gradient along x). In non-uniform open-channel flows, constant values of β along the longitudinal coordinate x, are a signature of equilibirum flows (Kironoto & Graf 1995), i.e. flows where appropriately-normalised vertical profiles of velocity statistics do not depend on the streamwise coordinate and can be therefore considered self-similar. Moreover, Kironoto & Graf (1995), Song & Chiew (2001) and Pu *et al.* (2018) indicate that in equilibrium open-channel flows, vertical profiles of velocity statistics are dependent on β. Therefore, it is important to estimate the variations of the parameter β, across all the experimental tests, to assess to what extent vertical profiles of velocity statistics measured at the test section are expected to collapse (or not) due to either lack of self-similarity or non-uniformity levels (i.e. local values of β).

Towards this end, the β parameter (equation 2.1) was estimated as follows: the free-surface water profile was approximated by linearly connecting each water depth measurement $h(x)$ provided by the ultrasonic gauges. This allowed for the estimation of four values of the water-surface gradient $S_w(x)$, which were considered representative of four cross-sections located halfway between two subsequent ultrasonic gauge positions, where the water depth $h(x)$ was also estimated. In equation 2.1, the shear velocity $u_\tau(x)$ was estimated from bulk momentum-balance principles as: $u_\tau = \sqrt{gS_fR_h}$, where $S_f = \mathrm{d}E/\mathrm{d}x$ is the energy-grade-line slope, E is the specific energy and R_h is the hydraulic radius.

The results are reported in figure 2. As can be seen, for each individual test, the parameter β varies at most of 7%, whereas, among all tests, β varies between -1.35 and -1.83. The literature pertaining to non-uniform open-channel flows (Kironoto & Graf 1995; Song & Chiew 2001; Pu *et al.* 2018) indicates that, such variations in β are associated with variations in second-order velocity statistics of less than 6% for each individual tests and 10% among all the tests. These variations are rather small and, as discussed in the next section, comparable to the relative error associated with the estimation of the shear velocity u_τ. It is therefore expected that appropriately-normalised profiles of velocity statistics pertaining to different tests should collapse with a general scatter of about 10%.

In support of the presence of self-similar flows, it is worth noting that test 4 and test 5 were conducted at two different test sections (i.e. 15 m and 30 m from the origin of the x coordinate, respectively) with very similar local values of β. When velocity statistics for the two tests were compared they displayed an excellent collapse (see figures in section 3.1).

2.3. *Estimation of the shear velocity*

The shear velocity is defined as $u_\tau = \sqrt{\tau_0/\rho}$, where τ_0 is the bed shear stress and ρ is the fluid density. The total shear stress τ_{tot} at any water depth for smooth-bed flow can be estimated as:

$$\frac{\tau_{tot}(y)}{\rho} = -\overline{u'v'}(y) + \nu\frac{\mathrm{d}U(y)}{\mathrm{d}y} \tag{2.2}$$

where, u' and v' are the longitudinal and vertical fluctuating velocity components, respectively, and over-bar stands for time-averaging. In uniform-flow conditions, τ_{tot} depends linearly on the vertical coordinate and hence τ_0 can be easily determined from extrapolation of τ_{tot}-profiles to the bed.

In non-uniform flows (as in the present case) the estimation of τ_0 and, consequently, of u_τ, is much more difficult because the dependence of τ_{tot} on the vertical coordinate is not known a-priori and any extrapolation of τ_{tot} to the bed can be affected by significant errors. For tests 1−2, things are further complicated by the fact that τ_{tot}-profiles might also be affected by the presence of secondary currents that, given the low aspect ratio of the tests, can contribute significantly to momentum transfer especially in the outer part of the flows.

At these conditions, it was decided to estimate u_τ by means of the Clauser method (Clauser 1956). Despite being based on fairly strong assumptions, the Clauser method is still widely used in turbulent wall-flows research (see e.g. Monty *et al.* 2009). The Clauser methods is based on the assumption that, in a flow region close to the wall, the vertical profile of the mean velocity follows a logarithmic behaviour. This hypothesis has been tested for uniform and non-uniform open-channel flows even at low aspect-ratios (Cardoso *et al.* 1989, 1991; Kironoto & Graf 1995; Kironoto 1998). The procedure adopted for quantifying the shear velocity for each test goes as follows. The classical logarithmic law for the longitudinal time-averaged mean velocity reads as:

$$U^+ = \frac{1}{\kappa}\ln\left(y^+\right) + B \tag{2.3}$$

where κ and B are the von Kàrmàn and the additive constant, respectively, and the superscript "+" refers to normalisation of lengths and velocities by means of the viscous length scale (ν/u_τ) and the shear velocity (u_τ), respectively. Assuming κ equal to 0.41, the

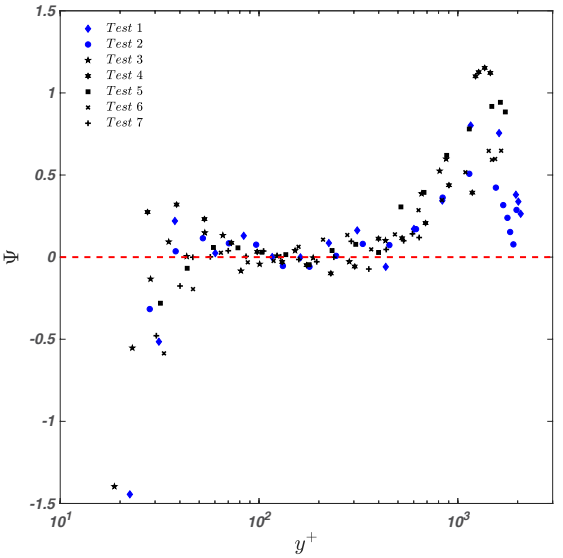


FIGURE 3. Variation of the Ψ function.

best fit between equation 2.3 and the experimental velocity data located above $y^+ = 50$ and below $y/h = 0.2$ provides the estimation for the shear velocity and B. In particular, an average value of B equal to 5.5 guarantees the most suitable collapse among all the velocity profiles. For better showing the reliability of the parameters obtained, we define the diagnostic function Ψ as the subtraction of equation 2.3 from the measured mean velocity profile as:

$$\Psi = U^+ - \frac{1}{\kappa} \ln\left(y^+\right) - B \tag{2.4}$$

In the logarithmic region, Ψ must exhibits values approximately equal to zero for the chosen values of B, κ and u_τ. Figure 3 demonstrates the good collapse of data within the range of elevations $50 \leqslant y^+ \leqslant 400$.

As shown in section 3.1, the estimated values of u_τ lead to a satisfactory collapse of first and second-order velocity moments. The values obtained for the constants κ and B well fall within the ranges identified by the literature pertaining to smooth-bed open-channel flows, i.e. $\kappa = 0.4 - 0.43$ and $B = 5 - 5.5$ (Steffler *et al.* 1985; Nezu & Rodi 1986; Kirkgöz 1989; Cardoso *et al.* 1989, 1991; Nezu & Nakagawa 1993; Kirkgöz & Ardiçlioğlu 1997; Roussinova *et al.* 2008; Onitsuka *et al.* 2009; Pu *et al.* 2018).

In order to substantiate the reliability of the procedure described above, the shear velocity u_τ was also estimated from bulk momentum-balance principles $u_\tau = \sqrt{gS_f h}$. These values were then corrected with the empirical formulation provided by Knight *et al.* (1984) to obtain values that are representative of the mid cross-section and hence comparable with those obtained from the Clauser method described above. Table 2 shows that the estimations of u_τ obtained from the two methods are in good agreement among all tests. Relative errors (%*R.E.*) are bounded between 1.6% and 4.9% except for test 1, whereby estimated values of u_τ deviate of about 9.7%. Taking a conservative approach, we conclude that the u_τ-values provided by the Clauser method, which are now used to scale velocity statistics presented in section 3, are subjected to an uncertainty of, at most, 10%.

Estimation Method	Test 1	Test 2	Test 3	Test 4	Test 5	Test 6	Test 7
Clauser Method	0.00985	0.01432	0.00755	0.01836	0.02016	0.02221	0.01518
Knight *et al.* (1984)	0.00890	0.01408	0.00742	0.01915	0.02091	0.02329	0.01597
$\%R.E.$	9.7	1.6	1.8	4.1	3.6	4.6	4.9

TABLE 2. Estimated values of u_τ (in m/s) at the mid cross-section using the Clauser method applied to the measured mean velocity profiles and the empirical approach by Knight *et al.* (1984). The last row of the table reports the percentage relative error $\%R.E.$ between the two estimates.

3. Results

3.1. *One point statistics*

Before addressing the issue of large-scale structures, an introductory section discussing classical one-point statistics is herein presented to validate the experimental methodology described in the previous section. This will be achieved by providing evidence that such statistics, when appropriately scaled, conform to data presented in the past literature. Furthermore, we believe that the following results might enrich the rather scarce set of published data on turbulence in smooth-bed open-channel flows and perhaps provide a benchmark for comparison with other canonical wall-flows.

Figure 4(a−d) reports the first and second-order velocity moments in classical inner scaling. Figure 4(a) reports the normalised longitudinal mean velocity profile together with the logarithmic law (equation 2.3). It can be seen that, although the Clauser method to estimate u_τ was applied to a fixed range of elevations contained between $y^+ = 50$ and $y/h = 0.2$ (as often done in wall-turbulence studies), the upper boundary of the log-region extends further away from the bed, i.e. up to $y/h = 0.35$ (this is best seen in Figure 5a).

Figure 4(b) and figure 4(c) report the non-dimensional standard deviation of the longitudinal (σ_u/u_τ) and bed-normal velocity component (σ_v/u_τ), respectively. Starting from $y^+ > 35$, figure 4(b) shows a systematic dependence of σ_u/u_τ on Re_τ, as already extensively observed both in open-channel flows (Nezu & Nakagawa 1993; Poggi *et al.* 2002) and in other wall-flows (Durst *et al.* 1995; De Graaff & Eaton 2000; Marusic *et al.* 2010; Smits *et al.* 2011).

The σ_v/u_τ profiles shown in figure 4(c) exhibit a plateau that increases its extent with increasing Re_τ. The σ_v/u_τ value at the plateau is about $1 - 1.11$, consistently with previous works on smooth-bed open-channel flows (Nezu & Nakagawa 1993; Poggi *et al.* 2002) as well as other wall-flows (Wei & Willmarth 1989; Durst *et al.* 1995).

The normalised Reynolds shear stress profiles $-\overline{u'v'}/u_\tau^2$ follow a similar trend (figure 4d) showing a plateau which increases in extent (along the vertical coordinate) with increasing Re_τ. The value of $-\overline{u'v'}/u_\tau^2$ at the plateau also increases with increasing Re_τ from 0.75 to 0.85, reflecting the weakening of the viscous shear stresses with increasing Reynolds number. This behaviour is also in good agreement with past literature on open-channel flow studies (Nezu & Nakagawa 1993; Poggi *et al.* 2002; Roussinova *et al.* 2008).

Figure 5(a−d) reports first and second-order velocity moments in classical outer scaling. For $y/h > 0.03$, mean velocity-defects $U_{max} - U$ collapse very well (figure 5a) on a curve described by the well-known logarithmic law in outer-scale normalisation:

$$\frac{U_{max} - U}{u_\tau} = -\frac{1}{\kappa} \ln\left(\frac{y}{h}\right) + B_1 \tag{3.1}$$

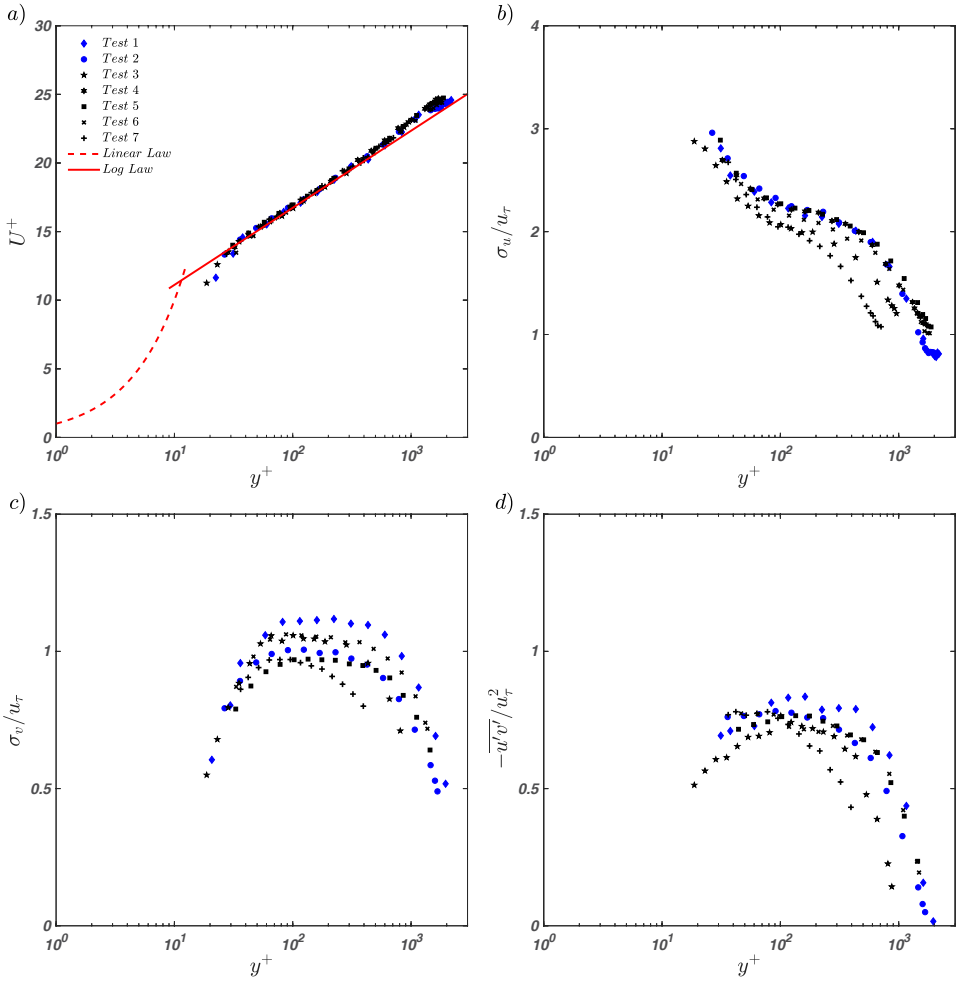


FIGURE 4. Inner scaling: (a) normalised streamwise mean velocity; (b) normalised standard deviation of the streamwise velocity fluctuations; (c) normalised standard deviation of the wall-normal velocity fluctuations; (d) normalised Reynolds shear stress. The dashed and continuous lines represent the linear and the log law of the wall.

where $B_1 = 0.5$ provides the best fit of the experimental data located at $y/h > 0.03$. In general, B_1 is related to the wake strength parameter Π as $B_1 = 2\Pi/\kappa$. Kironoto & Graf (1995) reports that the wake strength parameter retains a dependence on the non-uniformity parameter β as $\Pi = 0.08\beta + 0.23$. By using $\beta = -1.59$, which is the average taken over all the measured values of β reported in figure 2, Π results equal to 0.103, which compares very well with $\Pi = \frac{1}{2}\kappa B_1 = 0.102$ if $\kappa = 0.41$.

Normalised standard deviations and shear Reynolds stresses (figure 5b−d) collapse fairly well, although, with respect to mean velocities, they display a slightly higher level of scatter. However, it should be noted that most of the scatter occurs for $y/h > 0.5$ and is due to the data pertaining to tests 1 and 2. This was reasonably expected because these experiments are characterized by a low aspect ratio which makes velocity statistics susceptible to significant lateral-wall effects. Such effects are obviously expected to increase in significance with increasing distance from the bed. Focusing on the other high-aspect ratio experiments, the scatter is within 10%. As already discussed, this could

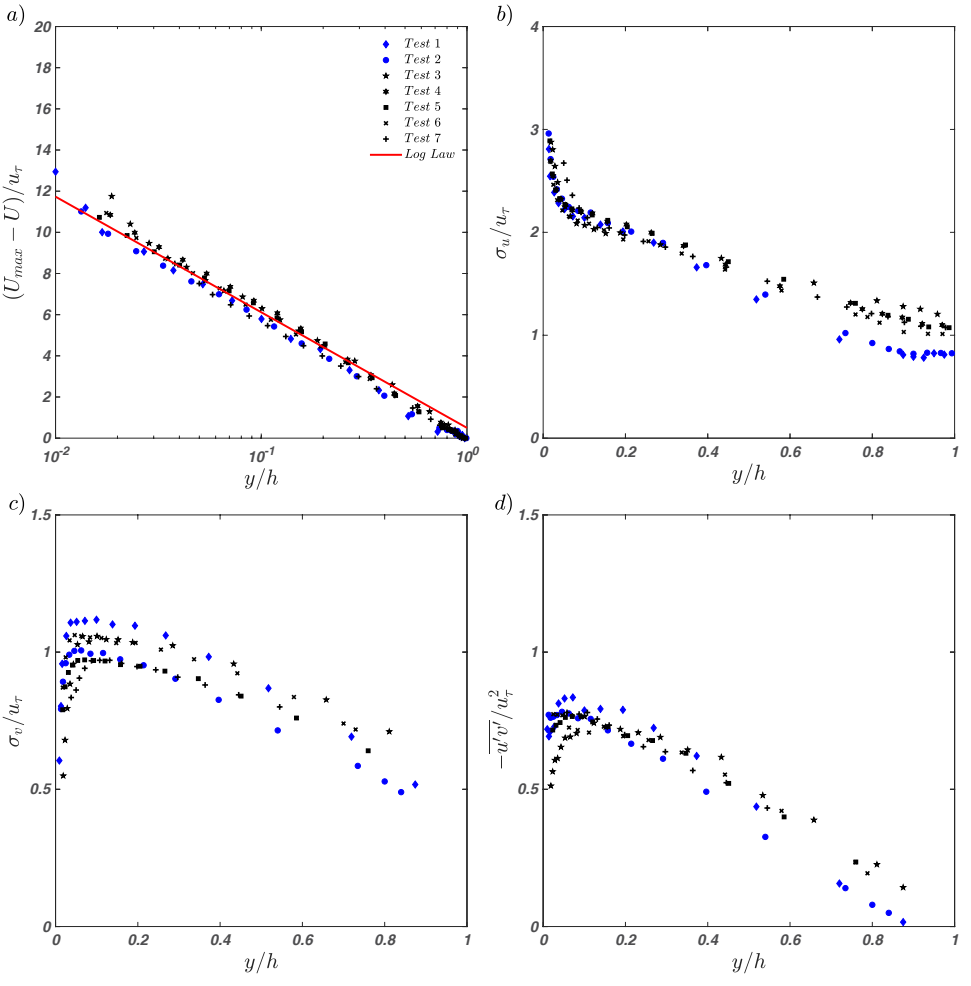


FIGURE 5. Outer scaling: (a) normalised streamwise mean velocity; (b) normalised standard deviation of the streamwise velocity fluctuations; (c) normalised standard deviation of the wall-normal velocity fluctuations; (d) normalised Reynolds shear stress. The continuous line is the velocity-defect law.

be due to either different values of the β parameter among the tests or to inaccuracy in the estimation of u_τ.

Figure 6(a−d) presents third and fourth-order standardised velocity moments (skewness and kurtosis) in usual outer-scale coordinates. Except for tests 1 and 2, which display a different behaviour, all the experimental data for $y/h > 0.2$ collapse in curves that resemble those published in the literature pertaining to open-channel flows over smooth walls (Poggi *et al.* 2002). With respect to the other tests, for $y/h > 0.4$, tests 1 and 2 are characterised by significantly-higher absolute values of skewness and kurtosis of both velocity components. The sign of S_u and S_v (figure 6a−b) suggests that ejection events in the outer layer are relatively more energetic in test 1 and 2 than in the other tests. Furthermore, the higher values of K_u and K_v indicate that such events occur rather intermittently (i.e. more intermittently than in the other tests). The authors do not have an argument to explain why low-aspect-ratios should trigger such a different

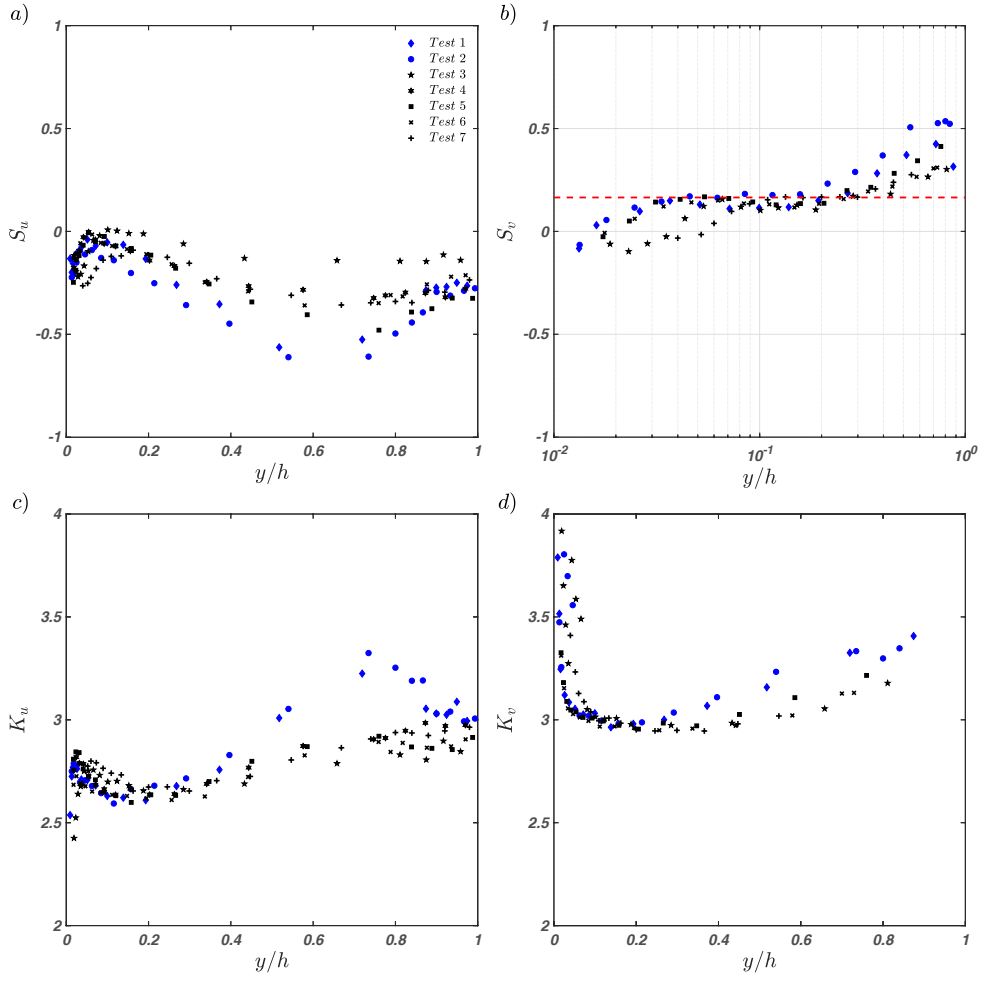


FIGURE 6. Measured (a) streamwise skewness; (b) wall-normal skewness; (c) streamwise kurtosis; (d) wall-normal kurtosis.

behaviour in terms of skewness and kurtosis so these results are left as the subject of future investigations.

It is interesting to note that, for all tests, the skewness of the vertical velocity component S_v displays a peculiar behaviour whereby a plateau of $S_v \approx 0.17$ occurs over a range of distances from the bed which increases in extent with increasing Re_τ but it is always bounded below $y/h = 0.2-0.3$ (figure 6b). As conjectured by Manes *et al.* (2011), the extent of the plateau and the way it depends on Re_τ share a lot in common with the overlap (logarithmic) layer of the mean velocities. This can be somewhat justified by the fact that S_v relates to part of the vertical turbulent flux of turbulent kinetic energy (i.e. the vertical turbulent transport of σ_v^2), which is expected to be constant in the overlap layer, where production and dissipation are in equilibrium (Townsend 1961; López & García 1999).

3.2. *Spectral analysis*

The one-dimensional (1-D) power spectral density of the longitudinal velocity component $E_{xx}(k_x)$ in the wavenumber domain can be estimated from its frequency counterpart

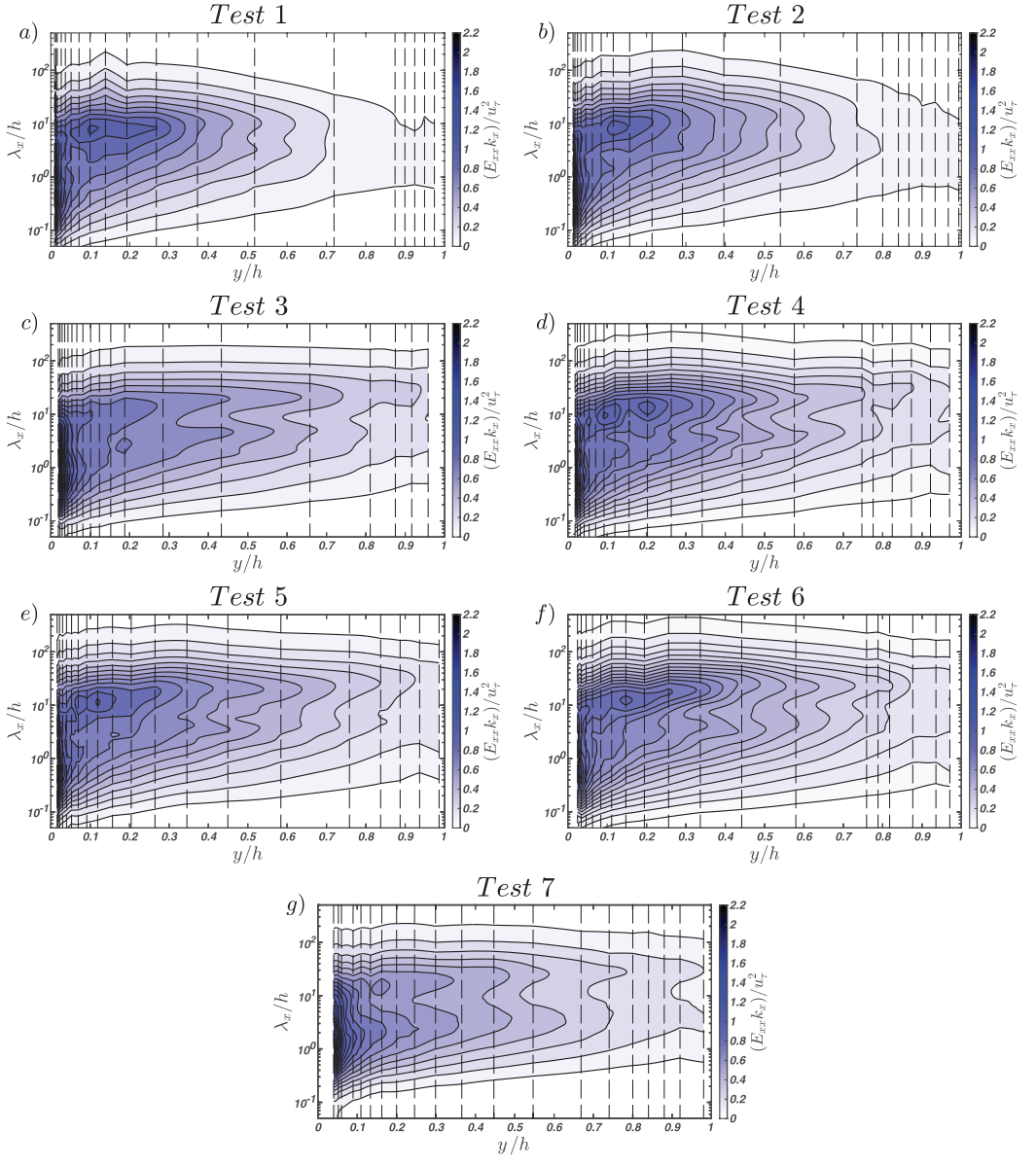


FIGURE 7. Contour maps of the outer-scaled pre-multiplied 1-D spectra of the longitudinal velocity component ($E_{xx}k_x/u_\tau^2$) as a function of non-dimensional streamwise wavelength (λ_x/h) and distance from the wall (y/h). The dashed lines indicate the bed-normal elevations where measurements were taken.

$E(f)$ by using the Taylor frozen-turbulence hypothesis (Taylor 1938). In particular, defining the streamwise wavenumber k_x as:

$$k_x = \frac{2\pi f}{U_c} \tag{3.2}$$

where f is the frequency and U_c is the eddy-convection velocity, the two power spectral densities are related by the following relation:

$$E_{xx}(k_x) = \frac{U_c}{2\pi} E(f) \tag{3.3}$$

In what follows, U_c was taken as the local mean velocity $U(y)$ at each elevation y of interest.

It is well-known that 1-D spectra suffer of aliasing effects (Tennekes & Lumley 1972), which artificially amplify the power spectral density of low frequency components. Further significant distortions may arise from the use of the Taylor hypothesis, when passing from the frequency to the wavenumber domain, especially when studying turbulence in the near-wall region (Kim & Adrian 1999; Guala *et al.* 2006; Del Álamo & Jiménez 2009; Cameron *et al.* 2017).

Despite these shortcomings, 1-D spectra have represented the key method to infer the scaling of large-scale structures in wall-flows and hence, to allow for a direct comparison with past studies, they are also employed in the present paper. In order to minimize the spectral distortion due to the adoption of Taylor's hypothesis, though, in what follows, results are discussed for the flow region above $y/h = 0.1$, where such distortion is significantly weaker than in the near-wall region (Nikora & Goring 2000). Results for $y/h < 0.1$ are reported for completeness but are not discussed in depth and should be taken with care.

In order to provide a comprehensive picture of the energy distribution among different length-scales, contour maps of pre-multiplied spectra are displayed in figure 7(a−g) for all the tests. The horizontal and vertical axes of each panel in figure 7 report the distance from the wall in outer-scaling y/h and the normalised wavelength λ_x/h, respectively (where $\lambda_x = 2\pi/k_x$).

Figure 7(a−g) demonstrates the existence of a double peak in the pre-multiplied spectra at wavelengths commensurate to those reported in the literature on wall-bounded flows for LSMs ($\lambda_x/h \approx \mathcal{O}(1)$) and VLSMs ($\lambda_x/h \approx \mathcal{O}(10)$).

For high aspect ratio experiments (i.e. tests 3, 4, 5, 6, and 7 with $W/h > 5$), the spectral footprint of both LSMs and VLSMs lasts up to and, in some cases, even beyond $y/h = 0.8$. This is at odds with what observed in turbulent boundary layers and duct (i.e. closed-channel and pipe) flows (Monty *et al.* 2009), where VLSMs disappear at much lower y/h. Indeed, in turbulent boundary layers and duct flows only LSMs persist beyond $y/\delta \approx 0.2$ (Adrian *et al.* 2000; Balakumar & Adrian 2007; Monty *et al.* 2009) and $y/\delta \approx 0.6$ (Guala *et al.* 2006; Monty *et al.* 2009), respectively. The double-peak persistency in open-channel flows was also reported by Cameron *et al.* (2017) and hence it seems to be a peculiarity of this class of flows.

The double peak is evident also for test 7 (figure 7g), which is characterized by a fairly low $Re_\tau = 725$. This result supports the findings of Wang & Richter (2019), who reports bimodal pre-multiplied spectra of the streamwise velocity component for Re_τ as low as 550. Once again this seems to be a peculiar characteristic of open-channel flows as, in canonical wall-flows, Hutchins & Marusic (2007*b*) identified a minimum $Re_\tau \approx 1700$ for the VLSM peak to clearly appear in pre-multiplied spectra.

Low aspect ratio experiments (i.e. tests 1 and 2 with $W/h < 5$) display some differences with respect to the other tests. In particular, the peak pertaining to VLSMs disappears at $y/h = 0.7$ and does not reach the water surface (figure 7a−b), as instead happens for tests 3−7 (figure 7c−g). Most importantly, λ_x/h for tests 1 and 2 are significantly smaller than in all other tests.

In order to have a clearer and general picture about the size and scaling of large-scale structures, figure 8 reports the wavelengths corresponding to spectral peaks pertaining to both LSMs and VLSMs for all experimental tests. Figure 8 also reports, for comparison,

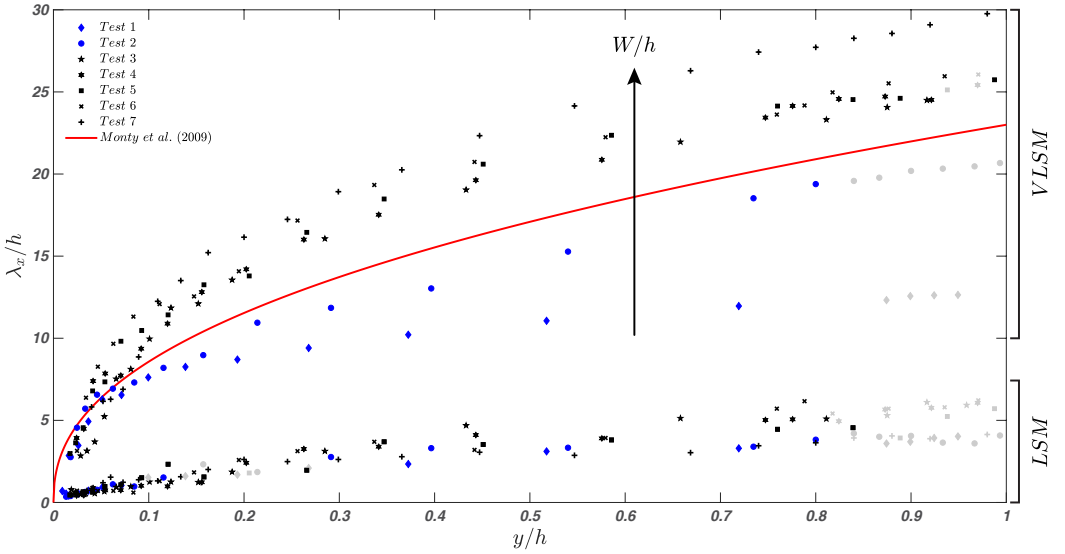


FIGURE 8. LSM and VLSM h-normalised wavelengths peaks in the pre-multiplied 1-D spectra of the longitudinal velocity component. The light grey markers indicate situations where LSM or VLSM peaks were not clearly detectable because poorly pronounced. The red line corresponds to the relation between normalised VLSM-wavelengths and normalised elevations proposed by Monty *et al.* (2009) for duct flows.

the empirical fit for VLSM-wavelengths proposed by Monty *et al.* (2009) for pipe and closed-channel flows i.e., $\lambda_x/\delta = 23\,(y/\delta)^{3/7}$ (where $\delta = h$ for open-channel flows).

There are a lot of interesting features that emerge from figure 8. We begin by pointing out that LSM-wavelengths scale well with the flow depth h regardless of flow conditions and resemble quite closely the results presented by Cameron *et al.* (2017). VLSMs' wavelengths, instead, do not scale with the flow depth h and are strongly dependent on the aspect ratio W/h. In fact, tests 3−6 which were carried out with a similar aspect ratio (i.e. spanning between approximately 5 and 7), are characterised by non-dimensional VLSMs' wavelengths λ_x/h collapsing well in one curve. Test 7, instead, shows results deviating significantly from such curve (especially for $y/h > 0.35$) and it was carried out at a much higher aspect ratio ($W/h \approx$12).

Perhaps the most interesting and striking result from figure 8 emerges from the data pertaining to the low aspect-ratio experiments, namely tests 1 and 2. The non-dimensional VLSM wavelengths pertaining to these tests decrease quite dramatically over a rather small variation of W/h between 4.07 (test 2) and 3.05 (test 1). Such wavelengths, also, drop well below the curve identified by Monty *et al.* (2009) for channel and pipe flows. On the contrary, LSM wavelengths keep scaling well with the flow depth h as for the other shallower flows.

One may argue that the effects of the aspect ratio W/h are not isolated in all these tests as also Re_τ and x/h vary extensively. A careful examination of the data, though, indicates that this is unlikely. For example, comparison between tests 4 and 5 allows to single out the effects of x/h (which varies extensively between 145 and 297) on VLSMs-scaling as W/h and Re_τ are kept reasonably constant. Figure 8 indicates that such effects are indeed negligible. As far as Re_τ is concerned, its effects are singled out reasonably well in tests 3−6 where it varies between $\approx$ 1000 and $\approx$ 1900. Again, the results from figure 8 indicate that, non-dimensional VLSMs wavelengths for all the other tests seem to be Re_τ-independent. Therefore, the only parameter that explains well the variations

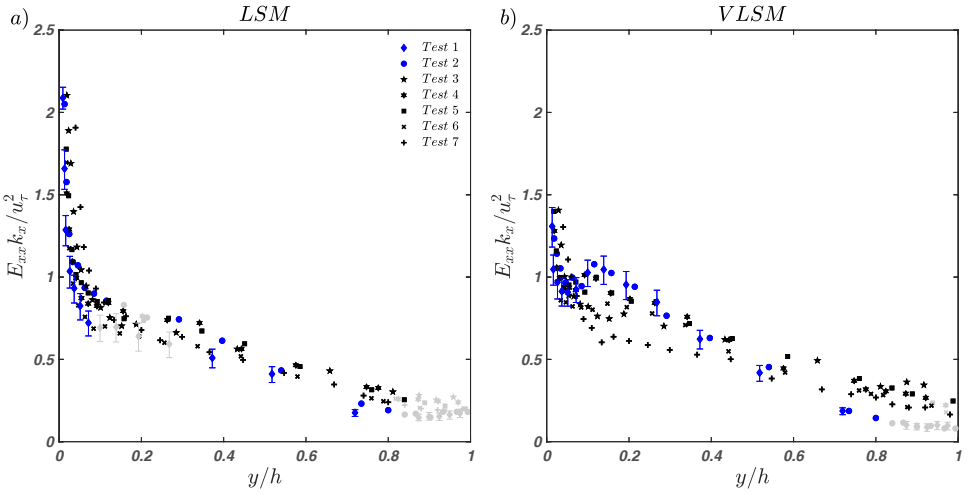


FIGURE 9. (a) Spectral energy associated with LSM peaks normalised with u_τ^2; (b) spectral energy associated with VLSM peaks normalised with u_τ^2. The light grey markers have the same meaning as described in figure 8. The error bars indicate the confidence interval bounds (with a 95% confidence level).

of VLSMs' wavelengths observed across all the tests is the aspect ratio W/h. This result provides further evidence to support the conjecture made by Cameron *et al.* (2017) that VLSMs and LSMs scale with different parameters. In particular, our data demonstrate unambiguously that, while LSMs scale well with the flow-depth, the size of VLSMs is dictated by the aspect ratio W/h. To further corroborate this result, 1-D spectra were also computed using the bulk velocity U_b (table 1) instead of the local velocity $U(y)$ in equations 3.2 and 3.3 and the final conclusions (not shown here) proved to be independent on the choice of the convection velocity.

For completeness, in figure 9(a−b) we also show the spectral energy associated with both LSM- and VLSM-peaks reported in figure 8. The 95% confidence interval for each spectral energy estimation is also provided to identify statistically significant differences between data. Since all data-points were characterised by very similar confidence intervals, these are reported only for one test to avoid figure overcrowding. In figure 9(a−b) the shear velocity squared provides a fairly good collapse of data, at least for $y/h > 0.4$. Below this level, namely for for $0.1 < y/h < 0.4$, the energy pertaining to LSM-peaks collapse very well for all tests (figure 9a). Instead, data-points related to VLSM-peaks seem to display some sort of stratification (figure 9b). It is difficult to discern whether this is dictated by Re_τ or the aspect ratio W/h. However, since tests 2 and 5 were carried out at very similar Re_τ (but very diferent W/h) and are characterized by the same energy in the VLSMs peaks, it can be reasonably argued that Re_τ-effects are more likely to dictate the stratification of data. This is also in line with results pertaining to canonical smooth-wall flows where the Re_τ-dependence of the VLSM-peaks energy has already been extensively reported (Marusic *et al.* 2010; Smits *et al.* 2011).

Given the significant dependence of VLSMs wavelengths on the aspect ratio W/h (see figure 8), it comes natural to associate VLSMs with cellular secondary currents, normally observed in open-channel flows. These secondary flows are, indeed, known to be dictated in number, size and intensity by the aspect ratio W/h and whose topological resemblance to VLSMs has already been suggested by various authors, so much so one could speculate that secondary currents are the footprint of VLSMs on the mean-flow (Adrian & Marusic

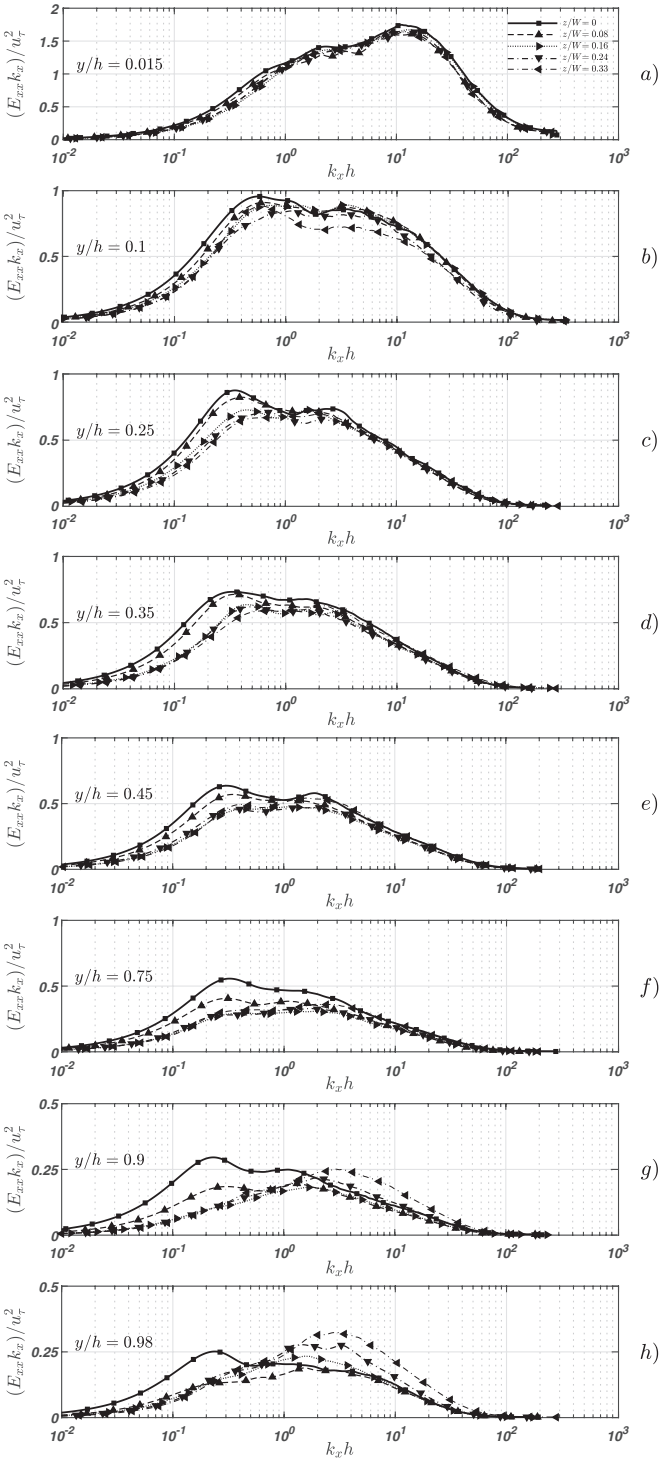


FIGURE 10. Pre-multiplied 1-D spectra of the longitudinal velocity fluctuations for tests 5−5d at eight different outer locations. Test 5 was measured in the centreline of the flume, while tests 5a, 5b, 5c and 5d were measured at $z/W = 0.08$, 0.16, 0.24 and 0.33, respectively. Panels (a)−(h) refer to spectra measured at different bed-normal elevations y/h. Note the different y-axes limits of panels (a), (g) and (h) with respect to the others.

2012). Secondary currents can be described as cells of longitudinal vorticity whose height and width is approximately equal to the flow depth and whose intensity decreases with increasing distance from the lateral walls. In close proximity of such walls, secondary cells are somewhat split and their structure altered significantly due to the presence of corners (Tominaga *et al.* 1989; Nezu & Nakagawa 1993; Wang & Cheng 2005; Rodríguez & García 2008).

On these premises, it becomes interesting to investigate the dependence of VLSMs' wavelengths (or wavenumbers) on the spanwise coordinate, because it represents a way of testing the response of VLSMs to variations in the structure and intensity of secondary currents, somewhat analogously to exploring VLSMs' dependence on the aspect ratio W/h. This is precisely what was investigated in experiments 5a−5d (table 1), whose results are reported in figure 10(a−h), where, each panel reports pre-multiplied spectra measured at a specific elevation from the bed and various locations along the spanwise coordinate. This figure indicates that for $y/h \geqslant 0.25$, the VLSM peak reduces in intensity and increases in wavenumber (i.e. reducing in wavelength) while approaching the lateral wall so much so in the proximity of the free-surface (i.e. $y/h = 0.98$, panel h) the VLSM peak occurs only in the central cross-section of the flow and disappears any closer to the lateral wall. This suggests that lateral walls and, presumably, associated effects on the structure and intensity of secondary currents, alter VLSMs. Furthermore, these observations point towards the idea that the observed W/h effects on VLSMs might be mediated by variations that W/h imposes on the intensity and size of secondary currents.

Note that as per VLSMs, the LSM peak also decreases in intensity while approaching the lateral wall but is not altered in wavenumber (see, in particular panels c, d, e and f) until $y/h \geqslant 0.9$ (see panels g and h) where, however, spectra display peaks that are probably the signature of coherent structures developing within the side-wall boundary layer.

4. Conclusions

A dataset of velocity measurements was collected in non-uniform, smooth-bed, open-channel flows over a wide range of hydraulic conditions. In order to validate the experimental methodology and assess the quality of the experimental data, classical one-point statistics obtained from measurements taken mostly in the mid cross-section of the flume, were first computed and discussed against literature data pertaining to open-channel flows and other canonical wall-flows. Results revealed that, provided the aspect ratio of the flow is greater than 5, velocity-profiles resemble those reported in the literature on open-channel flows and other canonical flows. In contrast, flows with aspect ratio lower than 5 display velocity-statistics profiles that are significantly affected by the lateral walls. As one would expect, such effects were observed to increase with increasing distance from the bed and prevented data to collapse with those pertaining to high aspect-ratio experiments. This was particularly evident for third and fourth order velocity statistics.

The key-results of the present work were obtained from spectral analysis of velocity time-series. Pre-multiplied 1-D spectra of the longitudinal velocity component revealed a double peak behaviour at wavenumbers consistent with those associated with LSMs and VLSMs, as observed in past studies on open-channel and canonical wall-flows. With respect to canonical wall-flows three key differences were observed: (i) the double peak behaviour persists throughout most of the vertical extension of the flow domain, namely up to at least $y/h = 0.8$, while in canonical wall-flows it disappears beyond $y/\delta = 0.6$ at most; (ii) the VLSM-peak appears in pre-multiplied spectra for Re_τ as low as 725, whereas in canonical wall-flows much higher values are known to be required (Hutchins &

Marusic 2007*b*); (iii) as argued by a recent study pertaining to uniform, rough-bed open-channel flows (Cameron *et al.* 2017), we confirm that the scaling of VLSMs-wavelengths is controlled by the aspect ratio W/h, as Re_τ and x/h effects were observed to be negligible. In particular, non dimensional VLSM-wavelengths resulted to increase with increasing W/h. We also confirm that LSM-wavelengths scale well with the outer length-scale of the flow, namely h.

For one hydraulic condition, vertical profiles of velocity time-series were measured not only in the mid cross-section of the flume but also at various positions along the spanwise coordinate z/W. Results from spectral analysis indicated that the wavelength and magnitude of the VLSM-peaks were much more dependent on the spanwise coordinate, than wavelengths pertaining to LSM-peaks. It was argued that, since in open-channel flows the shape and intensity of secondary currents also vary across the spanwise extent of the channel, the dynamics of VLSMs and secondary currents might be closely linked, as argued by Adrian & Marusic (2012).

Acknowledgements

C. Manes acknowledges the support of Compagnia di San Paolo through the grant scheme "Attrarre docenti di qualità dall'estero". C. Peruzzi is thankful to Teodoro Lamonaca, for the technical assistance in the realisation of the experimental set-up. The Associate Editor and the three anonymous Referees are gratefully acknowledged for their valuable comments. The authors report no conflict of interest.

REFERENCES

Adrian, R. J. 2007 Hairpin vortex organization in wall turbulence. *Phys. Fluids* **19** (4), 041301.

Adrian, R. J. & Marusic, I. 2012 Coherent structures in flow over hydraulic engineering surfaces. *J. Hydraul. Res.* **50** (5), 451–464.

Adrian, R. J., Meinhart, C. D. & Tomkins, C. D. 2000 Vortex organization in the outer region of the turbulent boundary layer. *J. Fluid Mech.* **422**, 1–54.

Bagherimiyab, F. & Lemmin, U. 2018 Large-scale coherent flow structures in rough-bed open-channel flow observed in fluctuations of three-dimensional velocity, skin friction and bed pressure. *J. Hydraul. Res.* **56** (6), 806–824.

Balakumar, B. J. & Adrian, R. J. 2007 Large-and very-large-scale motions in channel and boundary-layer flows. *Phil. Trans. R. Soc. Lond. A* **365** (1852), 665–681.

Bell, J. H. & Mehta, R. D. 1988 Contraction design for small low-speed wind tunnels. *NASA STI/Recon Technical Report N* **89**, 13753.

Cameron, S. M., Nikora, V. I. & Marusic, I. 2019 Drag forces on a bed particle in open-channel flow: effects of pressure spatial fluctuations and very-large-scale motions. *J. Fluid Mech.* **863**, 494–512.

Cameron, S. M., Nikora, V. I. & Stewart, M. T. 2017 Very-large-scale motions in rough-bed open-channel flow. *J. Fluid Mech.* **814**, 416–429.

Cameron, S. M., Nikora, V. I., Stewart, M. T. & Zampiron, A. 2018 Large and very large scale motions in rough-bed open-channel flow. *E3S Web of Conferences - River Flow 2018* **40** (05061).

Cardoso, A. H., Graf, W. H. & Gust, G. 1989 Uniform flow in a smooth open channel. *J. Hydraul. Res.* **27** (5), 603–616.

Cardoso, A. H., Graf, W. H. & Gust, G. 1991 Steady gradually accelerating flow in a smooth open channel. *J. Hydraul. Res.* **29** (4), 525–543.

Cellino, M. & Lemmin, U. 2004 Influence of coherent flow structures on the dynamics of suspended sediment transport in open-channel flow. *J. Hydraul. Res.* **130** (11), 1077–1088.

Chamorro, L. P., Hill, C., Morton, S., Ellis, C., Arndt, R. E. A. & Sotiropoulos, F.

2013 On the interaction between a turbulent open channel flow and an axial-flow turbine. *J. Fluid Mech.* **716**, 658–670.

Clauser, F. H. 1956 The turbulent boundary layer. *Adv. Appl. Math.* **4**, 1–51.

Cossu, C. & Hwang, Y. 2017 Self-sustaining processes at all scales in wall-bounded turbulent shear flows. *Phil. Trans. R. Soc. Lond. A* **375** (2089), 20160088.

Da Silva, A. M. F. & Yalin, M. S. 2017 *Fluvial processes: 2nd Edition*. CRC Press/Balkema, Leiden, The Netherlands.

Dantec Dynamics 2011 *LDA and PDA - Reference Manual*. Dantec Dynamics A/S, Skovlunde, Denmark.

De Graaff, D. B. & Eaton, J. K. 2000 Reynolds-number scaling of the flat-plate turbulent boundary layer. *J. Fluid Mech.* **422**, 319–346.

De Silva, C. M., Kevin, K., Baidya, R., Hutchins, N. & Marusic, I. 2018 Large coherence of spanwise velocity in turbulent boundary layers. *J. Fluid Mech.* **847**, 161–185.

Del Álamo, J. C. & Jiménez, J. 2003 Spectra of the very large anisotropic scales in turbulent channels. *Phys. Fluids* **15** (6), L41–L44.

Del Álamo, J. C. & Jiménez, J. 2009 Estimation of turbulent convection velocities and corrections to Taylor's approximation. *J. Fluid Mech.* **640**, 5–26.

Durst, F., Jovanović, J. & Sender, J. 1995 LDA measurements in the near-wall region of a turbulent pipe flow. *J. Fluid Mech.* **295**, 305–335.

Escudier, M. P., Nickson, A. K. & Poole, R. J. 2009 Turbulent flow of viscoelastic shear-thinning liquids through a rectangular duct: Quantification of turbulence anisotropy. *J. Nonnewton Fluid. Mech.* **160** (1), 2–10.

Franca, M. J. & Lemmin, U. 2015 Detection and reconstruction of large-scale coherent flow structures in gravel-bed rivers. *Earth Surf. Process. Landf.* **40** (1), 93–104.

Ganapathisubramani, B., Longmire, E. K. & Marusic, I. 2003 Characteristics of vortex packets in turbulent boundary layers. *J. Fluid Mech.* **478**, 35–46.

Ghesemi, A., Fox, J. & Husic, A. 2019 Predicting macroturbulence energy and timescales for flow over a gravel bed: Experimental results and scaling laws. *Geomorphology* **332**, 122–137.

Grinvald, D. I. & Nikora, V. I. 1988 *River turbulence*. Hydrometeoizdat, Leningrad, Russia.

Guala, M., Hommema, S. E. & Adrian, R. J. 2006 Large-scale and very-large-scale motions in turbulent pipe flow. *J. Fluid Mech.* **554**, 521–542.

Henderson, F. M. 1966 *Open channel flow*. Macmillan Publishing Co. Inc, New York, US.

Hommema, S. & Adrian, R. 2002 Similarity of apparently random structures in the outer region of wall turbulence. *Exp. Fluids* **33** (1), 5–12.

Hurther, D., Lemmin, U. & Terray, E. A. 2007 Turbulent transport in the outer region of rough-wall open-channel flows: the contribution of large coherent shear stress structures (LC3S). *J. Fluid Mech.* **574**, 465–493.

Hutchins, N., Hambleton, W. T. & Marusic, I. 2005 Inclined cross-stream stereo particle image velocimetry measurements in turbulent boundary layers. *J. Fluid Mech.* **541**, 21–54.

Hutchins, N. & Marusic, I. 2007*a* Evidence of very long meandering features in the logarithmic region of turbulent boundary layers. *J. Fluid Mech.* **579**, 1–28.

Hutchins, N. & Marusic, I. 2007*b* Large-scale influences in near-wall turbulence. *Phil. Trans. R. Soc. Lond. A* **365** (1852), 647–664.

Hutchins, N., Nickels, T. B, Marusic, I. & Chong, M. S. 2009 Hot-wire spatial resolution issues in wall-bounded turbulence. *J. Fluid Mech.* **635**, 103–136.

Hwang, Y. & Bengana, Y. 2016 Self-sustaining process of minimal attached eddies in turbulent channel flow. *J. Fluid Mech.* **795**, 708–738.

Hwang, Y. & Cossu, C. 2010 Self-sustained process at large scales in turbulent channel flow. *Phys. Rev. Lett.* **105** (4), 044505.

Hwang, Y., Willis, A. P. & Cossu, C. 2016 Invariant solutions of minimal large-scale structures in turbulent channel flow for Re_τ up to 1000. *J. Fluid Mech.* **802**.

Jackson, R. G. 1976 Sedimentological and fluid-dynamic implications of the turbulent bursting phenomenon in geophysical flows. *J. Fluid Mech.* **77** (3), 531–560.

Jiménez, J. 2018 Coherent structures in wall-bounded turbulence. *J. Fluid Mech.* **842**.

Jirka, G. H., Herlina, H. & Niepelt, A. 2010 Gas transfer at the air–water interface: experiments with different turbulence forcing mechanisms. *Exp. Fluids* **49** (1), 319–327.

Katul, G. G. 2019 The anatomy of large-scale motion in atmospheric boundary layers. *J. Fluid Mech.* **858**, 1–4.

Kim, K. C. & Adrian, R. J. 1999 Very large-scale motion in the outer layer. *Phys. Fluids* **11** (2), 417–422.

Kirkgöz, M. S. 1989 Turbulent velocity profiles for smooth and rough open channel flow. *J. Hydraul. Eng.* **115** (11), 1543–1561.

Kirkgöz, M. S. & Ardiçlioğlu, M. 1997 Velocity profiles of developing and developed open channel flow. *J. Hydraul. Eng.* **123** (12), 1099–1105.

Kironoto, B. A. 1998 The universality of the Kàrmàn constant on non-uniform open-channel flow. *11th Cong. of APD-IAHR* **2**, 579–586.

Kironoto, B. A. & Graf, W. H. 1995 Turbulence characteristics in rough non-uniform open-channel flow. *Proc., Instn. Civ. Engrs. Water, Maritime, and Energy* **112** (4), 336–348.

Knight, D. W., Demetriou, J. D. & Hamed, M. E. 1984 Boundary shear in smooth rectangular channels. *J. Hydraul. Eng.* **110** (4), 405–422.

López, F. & García, M. H. 1999 Wall similarity in turbulent open-channel flow. *J. Eng. Mech.* **125** (7), 789–796.

Manes, C., Poggi, D. & Ridolfi, L. 2011 Turbulent boundary layers over permeable walls: scaling and near-wall structure. *J. Fluid Mech.* **687**, 141–170.

Marusic, I., McKeon, B. J., Monkewitz, P. A., Nagib, H. M., Smits, A. J. & Sreenivasan, K. R. 2010 Wall-bounded turbulent flows at high Reynolds numbers: recent advances and key issues. *Phys. Fluids* **22** (6), 065103.

Monty, J. P., Hutchins, N., Ng, H. C. H., Marusic, I. & Chong, M. S. 2009 A comparison of turbulent pipe, channel and boundary layer flows. *J. Fluid Mech.* **632**, 431–442.

Monty, J. P., Stewart, J. A., Williams, R. C. & Chong, M. S. 2007 Large-scale features in turbulent pipe and channel flows. *J. Fluid Mech.* **589**, 147–156.

Moog, D. B. & Jirka, G. H. 1999 Air-water gas transfer in uniform channel flow. *J. Hydraul. Engng.* **125** (1), 3–10.

Nakagawa, H. & Nezu, I. 1981 Structure of space-time correlations of bursting phenomena in an open-channel flow. *J. Fluid Mech.* **104**, 1–43.

Nepf, H. M. 2012 Flow and transport in regions with aquatic vegetation. *Annu. Rev. Fluid Mec.* **44**, 123–142.

Nezu, I. 2005 Open-channel flow turbulence and its research prospect in the 21st century. *J. Hydraul. Engng.* **131** (4), 229–246.

Nezu, I. & Nakagawa, H. 1993 *Turbulence in Open-Channel Flows*. A. A. Balkema, Rotterdam, The Netherlands.

Nezu, I. & Rodi, W. 1986 Open-channel flow measurements with a Laser Doppler Anemometer. *J. Hydraul. Engng.* **112** (5), 335–355.

Nikora, V. I. & Goring, D. 2000 Eddy convection velocity and Taylor's hypothesis of 'frozen' turbulence in a rough-bed open-channel flow. *J. Hydrosci. Hydraul. Eng.* **18** (2), 75–91.

Onitsuka, K., Akiyama, J. & Matsuoka, S. 2009 Prediction of velocity profiles and reynolds stress distributions in turbulent open-channel flows with adverse pressure gradient. *J. Hydraul. Res.* **47** (1), 58–65.

Poggi, D., Katul, G. G., Albertson, J. D. & Ridolfi, L. 2007 An experimental investigation of turbulent flows over a hilly surface. *Phys. Fluids* **19** (3), 036601.

Poggi, D., Porporato, A. & Ridolfi, L. 2002 An experimental contribution to near-wall measurements by means of a special Laser Doppler Anemometry technique. *Exp. Fluids* **32** (3), 366–375.

Poggi, D., Porporato, A. & Ridolfi, L. 2003 Analysis of the small-scale structure of turbulence on smooth and rough walls. *Phys. Fluids* **15** (1), 35–46.

Pu, J. H., Tait, S., Guo, Y., Huang, Y. & Hanmaiahgari, P. R. 2018 Dominant features in three-dimensional turbulence structure: comparison of non-uniform accelerating and decelerating flows. *Environ. Fluid Mech.* **18** (2), 395–416.

Rashidi, M. 1997 Burst–interface interactions in free surface turbulent flows. *Phys. Fluids* **9** (11), 3485–3501.

Rashidi, M. & Banerjee, S. 1988 Turbulence structure in free-surface channel flows. *Phys. Fluids* **31** (9), 2491–2503.

Rawat, S., Cossu, C., Hwang, Y. & Rincon, F. 2015 On the self-sustained nature of large-scale motions in turbulent Couette flow. *J. Fluid Mech.* **782**, 515–540.

Robinson, S. K. 1991 Coherent motions in the turbulent boundary layer. *Annu. Rev. Fluid Mech.* **23** (1), 601–639.

Rodríguez, J. F. & García, M. H. 2008 Laboratory measurements of 3-D flow patterns and turbulence in straight open channel with rough bed. *J. Hydraul. Res.* **46** (4), 454–465.

Roussinova, V., Biswas, N. & Balachandar, R. 2008 Revisiting turbulence in smooth uniform open channel flow. *J. Hydraul. Res.* **46** (sup1), 36–48.

Roy, A. G, Buffin-Belanger, T., Lamarre, H. & Kirkbride, A. D. 2004 Size, shape and dynamics of large-scale turbulent flow structures in a gravel-bed river. *J. Fluid Mech.* **500**, 1–27.

Shen, C. & Lemmin, U. 1999 Application of an acoustic particle flux profiler in particleladen open-channel flow. *J. Hydraul. Res.* **37** (3), 407–419.

Shvidchenko, A. B. & Pender, G. 2001 Macroturbulent structure of open-channel flow over gravel beds. *Water Resour. Res.* **37** (3), 709–719.

Sillero, J. A., Jiménez, J. & Moser, R. D. 2014 Two-point statistics for turbulent boundary layers and channels at Reynolds numbers up $\delta^+ \approx 2000$. *Phys. Fluids* **26** (10), 105109.

Smits, A. J., McKeon, B. J. & Marusic, I. 2011 High–Reynolds number wall turbulence. *Annu. Rev. Fluid Mec.* **43**, 353–375.

Song, T. & Chiew, Y. M. 2001 Turbulence measurement in nonuniform open-channel flow using Acoustic Doppler Velocimeter (ADV). *J. Eng. Mech.* **127** (3), 219–232.

Steffler, P. M., Rajaratnam, N. & Peterson, A. W. 1985 LDA measurements in open channel. *J. Hydraul. Res.* **111** (1), 119–130.

Sukhodolov, A. N., Nikora, V. I. & Katolikov, V. M. 2011 Flow dynamics in alluvial channels: the legacy of Kirill V. Grishanin. *J. Hydraul. Res.* **49** (3), 285–292.

Tamburrino, A. & Gulliver, J. S. 1999 Large flow structures in a turbulent open channel flow. *J. Hydraul. Res.* **37** (3), 363–380.

Taylor, G. I. 1938 The spectrum of turbulence. *Proc. R. Soc. Lond. A* **164** (919), 476–490.

Tennekes, H. & Lumley, J. L. 1972 *A first course in turbulence*. MIT Press, Boston, US.

Tominaga, A., Nezu, I., Ezaki, K. & Nakagawa, H. 1989 Three-dimensional turbulent structure in straight open channel flows. *J. Hydraul. Res.* **27** (1), 149–173.

Tomkins, C. D. & Adrian, R. J. 2003 Spanwise structure and scale growth in turbulent boundary layers. *J. Fluid Mech.* **490**, 37–74.

Townsend, A. A. 1961 Equilibrium layers and wall turbulence. *J. Fluid Mech.* **11** (1), 97–120.

Trinci, G., Harvey, G. L., Henshaw, A. J., Bertoldi, W. & Hölker, F. 2017 Life in turbulent flows: interactions between hydrodynamics and aquatic organisms in rivers. *Wiley Interdiscip. Rev.: Water* **4** (3), e1213.

Venditti, J. G, Best, J. L., Church, M. & Hardy, R. J. 2013 *Coherent Flow Structures at Earth's Surface*. John Wiley & Sons, Chichester, UK.

Wang, G. & Richter, D. H. 2019 Two mechanisms of modulation of very-large-scale motions by inertial particles in open channel flow. *J. Fluid Mech.* **868**, 538–559.

Wang, Z. Q. & Cheng, N. S. 2005 Secondary flows over artificial bed strips. *Adv. Water Resour.* **28** (5), 441–450.

Wei, T. & Willmarth, W. 1989 Reynolds-number effects on the structure of a turbulent channel flow. *J. Fluid Mech.* **204**, 57–95.

Zhong, Q., Chen, Q., Wang, H., Li, D. & Wang, X. 2016 Statistical analysis of turbulent super-streamwise vortices based on observations of streaky structures near the free surface in the smooth open channel flow. *Water Resour. Res.* **52** (5), 3563–3578.

Zhong, Q., Li, D., Chen, Q. & Wang, X. 2015 Coherent structures and their interactions in smooth open channel flows. *Environ. Fluid Mech.* **15** (3), 653–672.